Scanning Probe Microscopy with Continuous Line Probe

Han-Wen Kuo*†, Anna Elisabeth Dorfi§¶, Daniel Esposito§¶ and John Wright*†‡

*Department of Electrical Engineering, Columbia University
†Data Science Institute, Columbia University
‡Department of Applied Physics and Applied Mathematics, Columbia University
§Department of Chemical Engineering, Columbia University
¶Columbia Electrochemical Energy Center and Lenfest Center for Sustainable Energy

***Abstract*—The principle of compressed sensing indicates that structured (sparse) signals can be reconstructed using far fewer measurements than traditional pointwise sampling schemes, provided those measurements are chosen to be incoherent with the basis of sparsity. In applications of scanning probe microscopy (SPM), images are acquired by raster scanning a point probe across a sample, to create an image. Viewed from the perspective of compressed sensing, this pointwise sampling scheme is inefficient, especially when the target image is structured. Replacing point measurements with delocalized, incoherent measurements has the potential to yield order-of-magnitude improvements in scan time. However, implementing the delocalized measurements of CS theory is challenging. In this paper we study a partially delocalized probe construction, in which the point probe is replaced with a continuous line, creating a sensor which essentially acquires line integrals of the target image. We show through simulations, rudimentary theoretical analysis, and experiments that these line measurements can image sparse samples far more efficiently than traditional point measurements. Despite this promise, practical reconstruction from line measurements poses additional difficulties: the measurements are partially coherent, and real measurements exhibit nonidealities. We show how to overcome these limitations using natural strategies (reweighting to cope with coherence, blind calibration for nonidealities), culminating in an end-to-end demonstration. Altogether, our results demonstrate the potential of combining a CS-like methodology with SPM, and show an example of how to redesign the reconstruction algorithm to cope with a measurement model that does not meet the theory.**

I. Introduction

Scanning probe microscopy (SPM) is a fundamental technique for imaging on a small scale based on interactions between a pointy probe and the sample of interest. Unlike traditional optical microscopy, the resolution achievable by SPM is not constrained by the diffraction limit, making SPM especially advantageous for nanoscale, or atomic level imaging, which has widespread applications in chemistry, biology and materials science [1].

Conventional implementations of SPM typically adopt a raster scanning strategy, which utilizes an probe with a small and sharp tip, to form a pixelated heatmap image via point-by-point measurements from interactions between the probe tip and the surface. Despite their capability of nanoscale imaging, SPM with pointwise measurement is inherently slow, especially when scanning a large area or producing high-resolution images.

When the target signal is highly structured, compressed sensing (CS) suggests it is possible to design a sampling scheme in which the number of measurements is largely dependent on the signal complexity, instead of the signal size, from which the signal can be efficiently reconstructed algorithmically. In nanoscale microscopy, images are often spatially sparse and structured. CS theory suggests for such signals, localized measurements such as pointwise samples are inefficient. In contrast, delocalized, spatially spread measurements are better suited to reconstructing a sparse image.

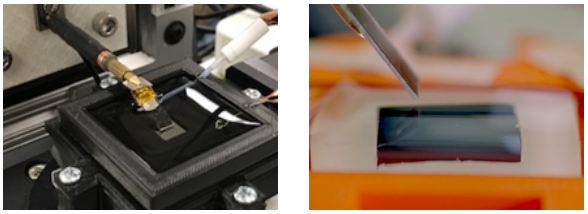

Fig. 1: Scanning electrochemical microscope with line probe. Left: the lab made SECM device with line probe. Mounted on an automated probe arms with a rotating sample stage. Right: closeup side view of the line probe near the sample surface.

However, in contrast to other practical implementations of CS, such as in MRI[2] or in fluorescence microscopy[3], which incorporate a spatially dense sampling pattern, in SPM it is hard to devise similar scanning method cost efficiently due to the probe manufacture limitations. This motivates us to study an implementation of SPM in which the probe is semi-localized, and is can be easily fabricated.

To this end, we study and implement the continuous line electrode probe (CLP)[4] for a specific type of SPM, called scanning electrochemical microscopy (SECM), which measures the chemical reaction between the probe and electroactive parts of the object[5], [6]. In SECM-CLP, the working end of the probe forms a straight line, produces a single measurement by collecting the accumulated current induced by interaction between the probe and the object surface. These *line probe* measurements are semi-localized, which samples spatially sparse image more efficiently then the pointwise measurements, and has great advantage for image resolution since a thin and sharp line probe can be easily manufactured.

Nevertheless, in practice, reconstructing an image from line scans faces two major challenges: (i) unlike measurement models in CS theory, the line scans are not incoherent to the spatially sparse signal, and (ii) the line probe has very unconventional point spread function comparing to point measurements. In this paper, we will discuss these challenges from the perspective of physical properties of line scans, and address how to reconstruct the microscopic images accordingly from our knowledge of these measurements. We conclude with real-data experiments demonstrating accurate reconstruction of a sparsely populated sample from line scans.

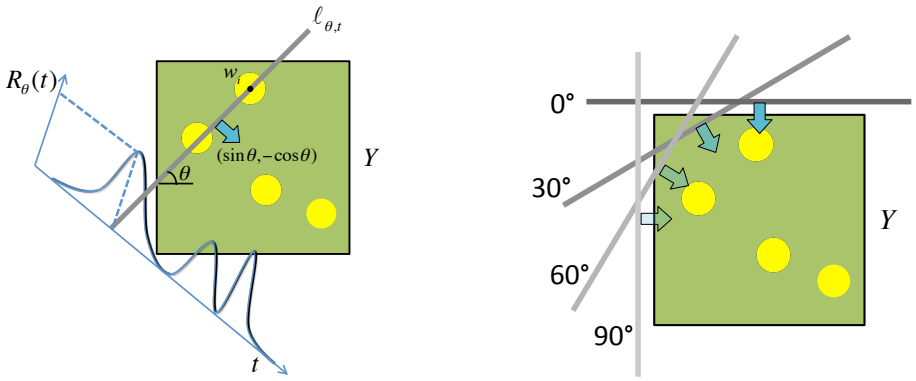

Fig. 2: Scanning procedure of SECM with continuous line electrode probe. (Left): A signal measurement from the line probe. The grey line in the figure represents the line probe, orienting in direction $\boldsymbol{u}_\theta = (\cos\theta, \sin\theta)$, and is sweeping in direction $\boldsymbol{u}_\theta^\perp = (\sin\theta, -\cos\theta)$. When it comes across the point $\boldsymbol{w}_i$ where $t = \langle \boldsymbol{u}_\theta^\perp, \boldsymbol{w}_i \rangle$, it integrates over the contact region $\ell_{\theta,t}$ between the probe and substate and produces a measurement $\boldsymbol{R}_\theta(t)$. Right: The complete line scans is done by sweeping the probe with different angles. In each sweeps, we measures equispaced samples.

II. Line scans measurement model

To implement the line scans for SECM, a line probe (Figure 1) is mounted on an automated arm which positions the probe onto the sample surface. The line scan signal is generated by placing this line probe in various places and angles, and measures the integrated current induced by the interaction between the line probe and the electroactive part of the sample. In a pragmatic scanning procedure (Figure 2, right), the user will elect distinct scanning angles, where in each scan of angle θ, the line probe is oriented in direction $\boldsymbol{u}_\theta = (\cos\theta, \sin\theta)$ and sweeps along the normal direction. Each of the sweep of probe generates a line, and the complete SECM line scans is the collection of lines of various scanning angles.

A. Line projection

Mathematically, we define a single line measurement from signal image with an ideal probe as the line integral of the image. When the probe body is oriented in direction $\boldsymbol{u}_\theta = (\cos\theta, \sin\theta)$ at position t (Figure 2, left), then the line integral of $\boldsymbol{Y}$ over the contacting surface between the probe and the object, is characterized as integration of $\boldsymbol{Y}$ over the line $\ell_{\theta,t}$, where the lines is defined as

$$\ell_{\theta,t} := \{\boldsymbol{w} \in \mathbb{R}^2 \,|\, \langle \boldsymbol{u}_\theta^\perp, \boldsymbol{w} \rangle = t\}, \tag{II.1}$$

and accordingly the line integral of $\boldsymbol{Y}$ at scanning angle θ and position t, $\mathcal{L}_\theta[\boldsymbol{Y}](t)$, can be characterized as

$$\begin{aligned} \mathcal{L}_\theta[\boldsymbol{Y}](t) &:= \int_{\ell_{\theta,t}} \boldsymbol{Y}(\boldsymbol{w})\, d\boldsymbol{w} \\ &:= \int_s \boldsymbol{Y}\left(s \cdot \boldsymbol{u}_\theta + t \cdot \boldsymbol{u}_\theta^\perp\right) ds. \end{aligned} \tag{II.2}$$

Operate the line integral of direction $\boldsymbol{u}_\theta$ across all locations t naturally forms a line $\mathcal{L}_\theta[\boldsymbol{Y}]$. In mathematics, the operation $\mathcal{L}_\theta : L^2(\mathbb{R}^2) \to L^2(\mathbb{R})$ projects the image onto a one dimensional line in direction $\boldsymbol{u}_\theta$, is known as the *line projection*.

A complete, ideal scans of image $\boldsymbol{Y}$ is the line projection in m directions of angles $\{\theta_i\}_{i=1}^m$, we denote the m-line projections as $\mathcal{L}_\Theta : L^2(\mathbb{R}^2) \to L^2(\mathbb{R} \times [m])$, which produces m different lines as

$$\begin{aligned} \mathcal{L}_\Theta[\boldsymbol{Y}] &:= \tfrac{1}{\sqrt{m}} \left[\mathcal{L}_{\theta_1}[\boldsymbol{Y}], \ldots, \mathcal{L}_{\theta_m}[\boldsymbol{Y}]\right] \\ &:= \tfrac{1}{\sqrt{m}} \textstyle\sum_{i=1}^m \mathcal{L}_{\theta_i}[\boldsymbol{Y}]\,. \end{aligned} \tag{II.3}$$

B. Line scans

For imaging systems in reality such as point probe microscope and focused optimal instruments, the point spread function (PSF) is often used to characterize the lowpass impulse response of the system due to the natural physical limitation. Similarly for line scans in practice, the spread effect of line probe blurs the line scan along its sweeping path, accordingly the actual line scans are modeled as the convolution between a one-dimensional PSF and the line projections.

Mathematically, we denote the PSF of line probe as $\boldsymbol{\psi}$ and the line projections $\{\mathcal{L}_{\theta_i}\}_{i=1}^m$, then the continuous line scans $\{\widetilde{\boldsymbol{R}}_i\}_{i=1}^m$ of an signal image $\boldsymbol{Y}$ can be characterized as

$$\widetilde{\boldsymbol{R}}_i = \tfrac{1}{\sqrt{m}} \boldsymbol{\psi} * \mathcal{L}_{\theta_i}[\boldsymbol{Y}], \qquad i = 1, \ldots, m; \tag{II.4}$$

and the collective m line scans of the image $\boldsymbol{Y}$ in all directions is denoted as

$$\widetilde{\boldsymbol{R}} = \tfrac{1}{\sqrt{m}} \textstyle\sum_{i=1}^m \boldsymbol{\psi} * \mathcal{L}_{\theta_i}[\boldsymbol{Y}] = \boldsymbol{\psi} * \mathcal{L}_\Theta[\boldsymbol{Y}]\,. \tag{II.5}$$

In SECM, the major characteristic of the PSF for line probe is it skews in one side and has a long tail in the sweeping direction. When the potential of probe is adjusted to a sufficiently negative value, it creates a diffusion layer of much greater size then the probe width. Electricity current is conducted as the layer contacts the electroactive species[6], causing a single line measurement from the species spreading in the direction of probe pathway. An instance of PSF of line probe in shown in Figure 3.

Finally the line scan measurement $\boldsymbol{R}_i = \mathcal{S}\{\widetilde{\boldsymbol{R}}_i\} \in \mathbb{R}^n$ is the n-equispaced samples of the continuous line $\widetilde{\boldsymbol{R}}_i$, and the collection of m discrete lines $\boldsymbol{R} = [\boldsymbol{R}_1, \ldots, \boldsymbol{R}_m] \in \mathbb{R}^{n \times m}$ is the observed signal from SECM-CLP device.

III. Promises and problems of line scans

The major component of the line scans, the line projections $\mathcal{L}_\theta$, enjoy two major advantages as an image sampling model: (i) comparing to the pointwise measurements, the line projections are more delocalized, hence can be more efficient when measuring a spatially sparse signal; and (ii) the sharp edge of the line probe is capable of detecting the directional high frequency components in the image.

Nevertheless, from a CS perspective, using line projection to sample a spatially sparse signal comes with an apparent disadvantage—the line measurements are not incoherent to the sparse signal representing bases. This means the number of sample required for exact reconstruction with line scans may not be optimal, it also is a cause for concern when image reconstruction, the conventional sparse recovery method may not lead to a satisfactory result.

As with most imaging systems, deblurring from the effect of PSF has always been an important and fundamental task for imaging algorithm. We will also demonstrate some example how PSF presents in the system of CLP, and address an algorithm solution to it in the next section.

A. Compressed sensing of line projections for highly localized image

Compressed sensing, in its simplest form, asserts that if the target signal has sparse representation, then only a few measurements that are incoherent to the representing basis will suffice for exact signal reconstruction. Since in many cases of microscopic imaging, the underlying signal is often structured and spatially localized, CS theory suggests the delocalized measurements, such as line projections, is more preferable then point measurements for more efficient scanning speed.

Specifically, when the signal image is highly spatially sparse and its sparse component are well separated, the line projections can be a very efficient measurement model. A concrete example is demonstrated in Lemma III.1, where we assume the sparse component of the image signal are small and separated discs; if the radius of the discs are sufficiently small, then, perhaps surprisingly, only three continuous line projections is required to exactly reconstruct the image.

Lemma III.1. *Consider an image consists of $\lambda \geq 2$ discs with centers are at least d-separated*[1]*. If the disc radius satisfies $R < Cd/(2\lambda^2)$, then three line scans with probe direction chosen independent uniformly at random suffice to recover the image with probability at least $1 - C$.*

Proof. See Section VI-B. ∎

B. Coherence between line projections and localized image in practice

While the microscopic images are often sparse in spatial domain, they rarely satisfy the conditions of Lemma III.1, in which local features are uncharacteristically small. The performance of line measurements can degrade when the size of the local feature increases. We will show this with a simple study of line scan measurement model.

Consider two different local feature profiles of different size $\boldsymbol{\delta}$ and $\boldsymbol{D}$, were $\boldsymbol{\delta}$ is a delta measure representing a profile with infinitesimally small diameter, and a disc profile $\boldsymbol{D}$ being appropriately sized. Comparing the coherence of the line projected profiles for the same feature at a pair of different location $\boldsymbol{w}_i, \boldsymbol{w}_j$ with projection angle randomly selected, then the profile with small diameter give

$$\mathbb{E}_\theta \left\langle \mathcal{L}_\theta[\boldsymbol{\delta}_{\boldsymbol{w}_i}], \mathcal{L}_\theta[\boldsymbol{\delta}_{\boldsymbol{w}_j}] \right\rangle = 0, \tag{III.1}$$

on the other hand, the average coherence with larger diameter can be approximated by

$$\mathbb{E}_\theta \left\langle \mathcal{L}_\theta[\boldsymbol{D} * \boldsymbol{\delta}_{\boldsymbol{w}_i}], \mathcal{L}_\theta[\boldsymbol{D} * \boldsymbol{\delta}_{\boldsymbol{w}_j}] \right\rangle \approx \left(1 + \tfrac{\|\boldsymbol{w}_i - \boldsymbol{w}_j\|_2^2}{\mathrm{diam}^2(\boldsymbol{D})}\right)^{-1/2} \tag{III.2}$$

[1]For data points $\boldsymbol{w}_1, \ldots, \boldsymbol{w}_\lambda$, the smallest distance between two points $\min_{i \neq j} \|\boldsymbol{w}_i - \boldsymbol{w}_j\|_2 \geq d$

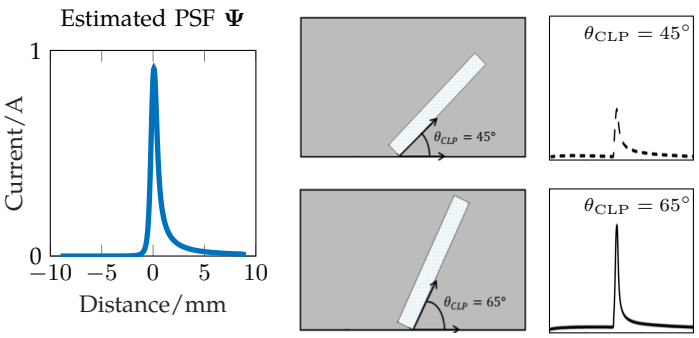

Fig. 3: The point spread function of line probe. The PSF of line probe is skewed in the probe sweeping direction. Left: an estimation of PSF of line probe with close form used for reconstruction, Right: a software simulated line scan PSF, when the contacting angle varies, the shape and intensity of PSF changes accordingly.

which, unsurprisingly, can be up to one when the profile is much larger then the the distances; even the two discs are separated, say $\mathrm{diam}(\boldsymbol{D}) \leq \|\boldsymbol{w}_i - \boldsymbol{w}_j\|_2$, the average coherence between the discs in line scans can still reach $1/\sqrt{2}$.

Due to the coherence phenomenon of line scans, we expect the number of line measurements for sparse recovery will not be as optimal as CS theory suggested; also, it will cause problems when operating image reconstruction with conventional sparse recovery method such as Lasso. We will address these issues by applying reweighting method in sparse recovery, which will elude with detail in the next section.

C. Stability of point spread function of line scans

Another major difference of CLP scans and the point probe measurements is the unique character of PSF. In some cases, the PSF can be structurally different due to some physical phenomenon from scanning procedure. For instance in Figure 3 right, we show when the contacting angle between the probe and the sample varies, the corresponding PSF changes drastically in both magnitude and shape, which has been one of the main source of error during reconstruction in our experience.

A remedy of the instability of PSF, is to parameterize the PSF to accommodate all possible variations. In Figure 3 left, we demonstrate an instance of estimated PSF, in which the shape and size can be calibrated in the course of optimization during image reconstruction. We will show an example when the PSF is varying from each line scans, how is this approach reconstruct image from unstable measurements.

IV. Reconstruction of localized signal from line scans

A. Sparse recovery with Lasso for ideal signal

In the following experiments, we will consider a representative class of image, whose electroactive heatmap $\boldsymbol{Y}$ can be characterized as several superposed reactive species $\boldsymbol{D}$ appearing at different locations $\mathcal{W} = \{\boldsymbol{w}_j\}_{j=1}^{|\mathcal{W}|} \subseteq \mathbb{R}^2$ with each of its heatmap intensity denoted as $\{\alpha_j\}_{j=1}^{|\mathcal{W}|} \subseteq \mathbb{R}_+$ (Figure 4). Define the activation map as $\boldsymbol{X}_0 = \sum_{j=1}^{|\mathcal{W}|} \alpha_j \boldsymbol{\delta}_{\boldsymbol{w}_j}$ which encodes the locations and intensities of $\boldsymbol{D}$ as summation of $|\mathcal{W}|$ discrete

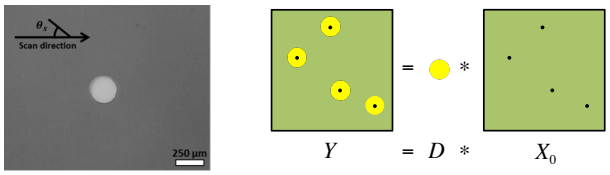

Fig. 4: Signal model of superposing electroactive species at different location. Left: a closeup for single electroactive disc $\boldsymbol{D}$. Right: the heatmap image of the substate $\boldsymbol{Y}$ is convolution between electroactive species $\boldsymbol{D}$ and its activation map $\boldsymbol{X}_0$.

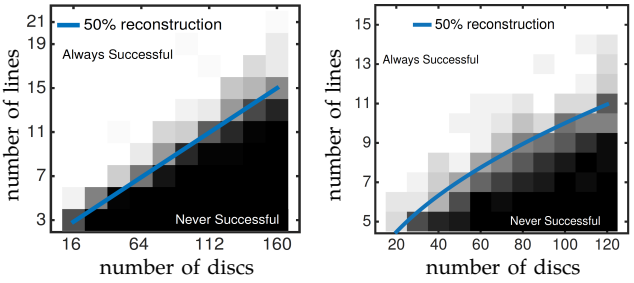

Fig. 5: Phase transition of fixed image size (left) and fixed density (right) on support recovery with Lasso. Each pixel is the average of 50 experiments.

Dirac measures $\boldsymbol{\delta}_{\boldsymbol{w}}$[2], then the image $\boldsymbol{Y}$ can simply be written as the convolution between the species $\boldsymbol{D}$ and measure $\boldsymbol{X}_0$:

$$\boldsymbol{Y} = \boldsymbol{D} * \boldsymbol{X}_0 = \textstyle\sum_{j=1}^{|\mathcal{W}|} \alpha_j \boldsymbol{D} * \boldsymbol{\delta}_{\boldsymbol{w}_j}. \tag{IV.1}$$

Then the imaging reconstruction problem can be cast as finding the best fitting sparse map discretized sparse map $\widehat{\boldsymbol{X}}$ from line scans $\boldsymbol{R} = \mathcal{S}\{\boldsymbol{\Psi} * \mathcal{L}_\Theta[\boldsymbol{D} * \boldsymbol{X}_0]\}$, in which the reconstructed image will be $\boldsymbol{D} * \widehat{\boldsymbol{X}}$.

Notice that the discrete samples, the convolution and the line projections are all linear, hence the operator from the map $\boldsymbol{X}_0$ to the lines $\boldsymbol{R}$ is also linear. A natural method to solve for $\boldsymbol{X}_0$ is by minimizing the lasso objective under the line scan measurement model.

$$\min_{\boldsymbol{X} \geq 0} \lambda \textstyle\int |d\boldsymbol{X}| + \frac{1}{2} \left\| \boldsymbol{R} - \mathcal{S}\{\boldsymbol{\Psi} * \mathcal{L}_\Theta[\boldsymbol{D} * \boldsymbol{X}]\} \right\|_2^2. \tag{IV.2}$$

We study the performance of discretized version of (IV.2) where $\boldsymbol{X}_0$ is assume to be supported on the grid, and the PSF to be an ideal delta function. Figure 5 shows the reconstruction performance when with synthetic data were generated by randomly allocated discs of 100 μm in diameter and center-to-center are separated by 50 μm. The number of line scans required in both scenario (fix area/fix density) are lower when fewer discs are present, showing that when signal is sparser, the line scans indeed is more efficient then the point probe.

B. Reweighted Lasso for coherent measurement

To study how the coherence of line scans affects image reconstruction, ignore the discrete sampler and consider the continuous lines scans, we define the $\boldsymbol{G} \in \mathbb{R}^{|\mathcal{W}|}$ as the Gram matrix of linear map $\mathcal{L}_\Theta[\boldsymbol{D} * \cdot]$ at locations $\mathcal{W}$ as

$$\boldsymbol{G}_{ij} := \left\langle \boldsymbol{\psi} * \mathcal{L}_\Theta \left[\boldsymbol{D} * \boldsymbol{\delta}_{\boldsymbol{w}_i}\right], \boldsymbol{\psi} * \mathcal{L}_\Theta \left[\boldsymbol{D} * \boldsymbol{\delta}_{\boldsymbol{w}_j}\right] \right\rangle \tag{IV.3}$$

[2]The Dirac measure satisfies $\int \boldsymbol{D}(\boldsymbol{w}) \boldsymbol{\delta}_{\boldsymbol{w}_i}(d\boldsymbol{w}) = \boldsymbol{D}(\boldsymbol{w}_i)$ for any continuous and compactly supported $\boldsymbol{D}$. And has total variation $\int |\boldsymbol{\delta}_{\boldsymbol{w}_i}| (d\boldsymbol{w}) = 1$, see [7].

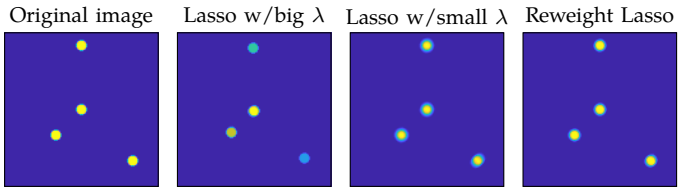

Fig. 6: SECM image reconstruction with pure lasso and reweighted lasso. We apply three algorithm to reconstruct the image (left) with 6 line scans with simulated PSF in Figure 3. The reconstruction from lasso with large λ (mid left) has unbalanced magnitude due to the coherence of line scans, and from lasso with small λ (mid right) gives blurry image by weakened sparsity regularizer. Reweighing lasso can adjust the sparse regularizer in each iteration and consistently gives good result.

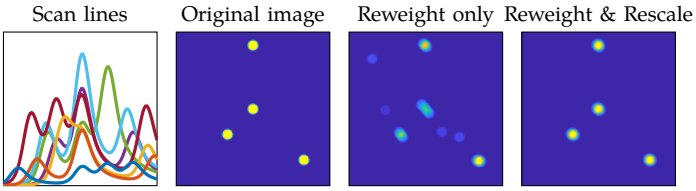

Fig. 7: SECM image reconstruction with pure lasso and reweighted lasso. We simulate a line scan with uneven magnitude (left), and reconstruct the image (mid left) with two algorithm. The algorithm with reweighting only (mid right) cannot identify the correct support; where the reweighting plus calibration (right) method receives good result.

and the solution $\boldsymbol{X}$ of program (IV.2) on $\mathcal{W}$ can be written as

$$\boldsymbol{X}_{\mathcal{W}} = \boldsymbol{X}_{0\mathcal{W}} - \lambda \boldsymbol{G}^{-1} \boldsymbol{1}. \tag{IV.4}$$

Since the line scans is coherent for $\mathcal{W}$, many entries of $\boldsymbol{G}$ will has a large, positive number sometime close to the diagonal entry, hence $\boldsymbol{G}$ can sometimes be very ill-conditioned. When λ is large, this will cause the solution of $\boldsymbol{X}$ from Lasso has unfavorable solutions (Figure 6).

We apply reweighting strategy[8], iteratively solves the objective with updated $\lambda_{ij}^{(k)} \leftarrow (\boldsymbol{X}_{ij}^{(k-1)} + \varepsilon)^{-1}$ at k-th iterate.

C. Image reconstruction algorithm from line scans

Since the PSF can has varying between each line scans, we calibrate it via optimizing these parameters $p \in \mathcal{P}$ and solve it using the iPalm algorithm[9]. We recover $\boldsymbol{Y}$ by solving discretized $\boldsymbol{X} \in \mathbb{R}^{n \times n}$ which approximates $\boldsymbol{X}_0$ by minimizing Lasso-type objective:

$$\begin{aligned} \min_{\boldsymbol{X} \geq 0, p \in \mathcal{P}} & \textstyle\sum_{i,j=1}^{n} \lambda_{ij} \boldsymbol{X}_{ij} \\ & + \textstyle\sum_{i=1}^{m} \frac{1}{2} \left\| \mathcal{S}\{\boldsymbol{\psi} * \mathcal{L}_{\theta_i}\{\boldsymbol{p}_i\}[\boldsymbol{D} * \boldsymbol{X}]\} - \boldsymbol{R}_i \right\|_2^2 \end{aligned} \tag{IV.5}$$

V. Real data experiments

We present two sets of experiments in Figure 8 and Figure 9 to demonstrate an end-to-end result of SECM-CLP with algorithmic reconstruction.

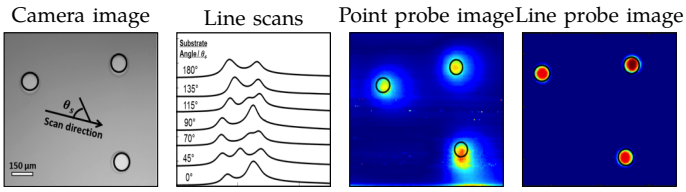

Fig. 8: Real signal experiments for 3 dots [10]. In which we show the comparison with point probe, where with line probe we can more accurately locate the position of the dot, even compare to the point probe.

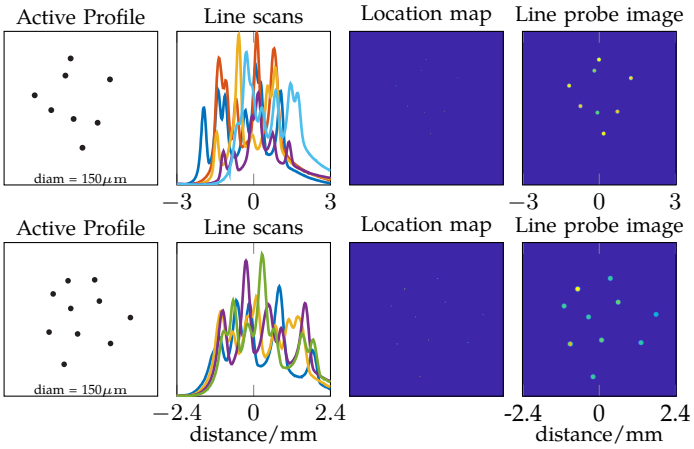

Fig. 9: Real signal experiments for 8, 10 dots. Here we show our algorithm can reconstruct a slightly more complicated signal, where 8,10 dots are presented. Our algorithm successfully reconstruct the image, with the sparse location map close to discrete. The image resolution is 10μm in each pixels.

VI. Summary & Discussion

We develop a novel scanning probe microscope technique involving the use of line probe on from design of the device and the algorithm. It operates line integral for each measurement, enables non-local measurement for sparse recovery in practice, which speeds up the microscopic for image with localized sparse structure. Despite the existence of some nonidealities of line scans, we can successfully reconstruct image with algorithmic approach.

Appendix

A. Adjoint of line projection

The adjoint operator[3] of line projections $\mathcal{L}_\Theta^* : L^2([m]\times\mathbb{R}) \to L^2(\mathbb{R}^2)$ is deeply connected with the well-known tomography image reconstruction technique *back projection*. The adjoint of a single line projection $\mathcal{L}_{\theta_i}^* : L^2(\mathbb{R}) \to L^2(\mathbb{R}^2)$ of scanning angle θ_i is the back projection of a line scan $\boldsymbol{R}_i$ generates an image whose value over $\ell_{\theta_i,t}$ is equivalent to $\boldsymbol{R}_i(t)$:

$$\mathcal{L}_{\theta_i}^*[\boldsymbol{R}_i](\boldsymbol{w}) = \boldsymbol{R}_i(t), \qquad \forall\, \boldsymbol{w} \in \ell_{\theta_i,t}, \tag{VI.1}$$

[3]We invoke the canonical definition of inner product of L^2-space for both image and lines. For any $\boldsymbol{Y}, \boldsymbol{Y}' \in L^2(\mathbb{S}^1)$, then $\langle \boldsymbol{Y}, \boldsymbol{Y}'\rangle = \int \boldsymbol{Y}(\boldsymbol{w})\boldsymbol{Y}'(\boldsymbol{w})\,d\boldsymbol{w}$; and for any $\boldsymbol{R}, \boldsymbol{R}' \in L^2(\mathbb{R}\times[m])$, we have $\langle \boldsymbol{R}, \boldsymbol{R}'\rangle = \sum_{i=1}^m \int \boldsymbol{R}_i(t)\boldsymbol{R}_i'(t)\,dt$.

then incorporate with definition of $\ell_{\theta_i,t}$ in (II.1), we obtain a simpler form for $\mathcal{L}_{\theta_i}^*$ as

$$\mathcal{L}_{\theta_i}^*[\boldsymbol{R}_i](\boldsymbol{w}) = \boldsymbol{R}_i(\langle \boldsymbol{u}_{\theta_i}^\perp \boldsymbol{w}]\rangle). \tag{VI.2}$$

Extending the derivation of (VI.2) to m-lines $\boldsymbol{R}$, on which we apply back projection $\mathcal{L}_\Theta^*$ and gain an image as the superposition of all m back projected lines of different scanning angles.

$$\begin{aligned}\mathcal{L}_\Theta^*[\boldsymbol{R}](\boldsymbol{w}) &= \tfrac{1}{\sqrt{m}}\textstyle\sum_{i=1}^m \mathcal{L}_{\theta_i}^*[\boldsymbol{R}_i](\boldsymbol{w}) \\ &= \tfrac{1}{\sqrt{m}}\textstyle\sum_{i=1}^m \boldsymbol{R}_i(\langle \boldsymbol{u}_{\theta_i}^\perp, \boldsymbol{w}\rangle).\end{aligned} \tag{VI.3}$$

In the following proposition, we show that the line projections defined in (VI.3) is indeed the adjoint operator of line projections.

Proposition VI.1. *The back projection $\mathcal{L}_\Theta^*$ in (VI.3) is the adjoint of line projection $\mathcal{L}_\Theta$ in (II.3), where*

$$\langle \boldsymbol{R}, \mathcal{L}_\Theta[\boldsymbol{Y}]\rangle = \langle \mathcal{L}_\Theta^*[\boldsymbol{R}], \boldsymbol{Y}\rangle\,. \tag{VI.4}$$

Proof. For any lines $\boldsymbol{R} \in L^2([m]\times\mathbb{R})$ image $\boldsymbol{Y} \in L^2(\mathbb{S}^1)$, and any angles $\Theta = \{\theta_1, \dots, \theta_m\}$,

$$\begin{aligned}\langle \boldsymbol{R}, \mathcal{L}_\Theta[\boldsymbol{Y}]\rangle &= \tfrac{1}{\sqrt{m}}\textstyle\sum_{i=1}^m \int \boldsymbol{R}_i(t)\mathcal{L}_{\theta_i}[\boldsymbol{Y}](t)\,dt \\ &= \tfrac{1}{\sqrt{m}}\textstyle\sum_{i=1}^m \int \boldsymbol{R}_i(t)\int \boldsymbol{Y}(s\boldsymbol{u}_{\theta_i} + t\boldsymbol{u}_{\theta_i}^\perp)\,ds\,dt \\ &= \tfrac{1}{\sqrt{m}}\textstyle\sum_{i=1}^m \int \boldsymbol{R}_i\left(\langle \boldsymbol{w}, \boldsymbol{u}_{\theta_i}^\perp\rangle\right)\boldsymbol{Y}(\boldsymbol{w})\,d\boldsymbol{w} \\ &= \int \left(\tfrac{1}{\sqrt{m}}\textstyle\sum_{i=1}^m \boldsymbol{R}_i\left(\langle \boldsymbol{w}, \boldsymbol{u}_{\theta_i}^\perp\rangle\right)\right)\boldsymbol{Y}(\boldsymbol{w})\,d\boldsymbol{w} \\ &= \langle \mathcal{L}_\Theta^*[\boldsymbol{R}], \boldsymbol{Y}\rangle\,.\end{aligned} \tag{VI.5}$$

The first equality comes from the definition of inner product in lines space; the second comes from (**??**); the third uses change of variable where $\boldsymbol{w} = s\boldsymbol{u}_\theta + t\boldsymbol{u}_\theta^\perp$ for every θ; the fourth comes from linearity; and the last equality from definition of inner product in image space. ∎

B. Proof of Lemma III.1

Proof. We first argue that with high probability, no pair of discs overlaps within any line scan. Let $\theta_j \sim_{\text{i.i.d.}} \text{Unif}[-\pi, \pi)$ denote the j-th scanning angle. The probability that any particular pair of two discs overlap is bounded as

$$\begin{aligned}&\mathbb{P}\left[\text{Two dots overlap on line scan } \boldsymbol{R}_j\right] \\ &\quad\le \mathbb{P}\left[\theta_i \in \left[-\sin^{-1}\left(\tfrac{2R}{d}\right), \sin^{-1}\left(\tfrac{2R}{d}\right)\right]\right] \\ &\quad= \tfrac{2}{\pi}\sin^{-1}\tfrac{2R}{d}\end{aligned} \tag{VI.6}$$

Using the assumption that $R < \frac{d}{8}$ to bound $\sin^{-1}(\frac{2R}{d}) < \frac{2\pi R}{3d}$ and summing the failure probability over all three line scans and $\frac{\lambda(\lambda-1)}{2}$ pairs of dots, we obtain:

$$\begin{aligned}&\mathbb{P}\left[\text{Two of the } \lambda \text{ dots overlap at either } \boldsymbol{R}_1, \boldsymbol{R}_2, \boldsymbol{R}_3\right] \\ &\quad\le \tfrac{3\lambda^2}{2}\cdot\tfrac{2}{\pi}\mathbb{P}\left[\text{Two dots overlap on line scan } \boldsymbol{R}_1\right] \\ &\quad\le \tfrac{3\lambda^2}{\pi}\sin^{-1}\left(\tfrac{2R}{\lambda}\right) \\ &\quad\le \tfrac{2\lambda^2 R}{d} \\ &\quad\le C\end{aligned} \tag{VI.7}$$

Thus, with probability at least $1 - C$, no pair of discs overlaps in any line scan.

Since there are no overlapping dots in any line, a single line scan $\boldsymbol{R}(t)$ with scan angle θ has largest magnitude at points t where the probe body passes the center of a disc. These points

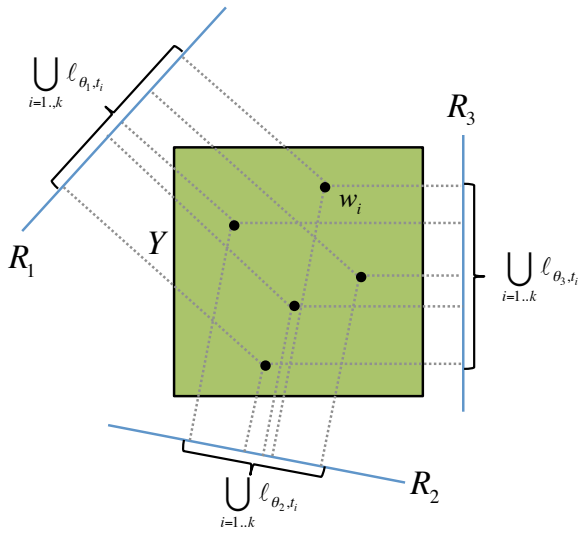

Fig. 10: Proof idea for sufficiency of identifying disc location via three line scans. The grey dashed lines are back projection lines, forming the set $\cup_{i=1}^{\lambda} \ell_{(\theta,\boldsymbol{w})}$. Intersection of three such line sets is exactly the set of dot centers, which generate the peak measurements in $\boldsymbol{R}_1, \boldsymbol{R}_2$ and $\boldsymbol{R}_3$.

of largest magnitude can be written as $\left\{\left\langle \boldsymbol{u}_\theta^\perp, \boldsymbol{w}_i \right\rangle, i = 1, \ldots, \lambda\right\}$ on $\boldsymbol{R}$. Using these points, for every location $\boldsymbol{w}_i$ and angle θ, we define a back projected line $\ell_{\theta,\boldsymbol{w}_i}$ as a subset of $\mathbb{R}^2$, where

$$\ell_{\theta,t_i} := \{\boldsymbol{w} \in \mathbb{R}^2 \,|\, \langle \boldsymbol{u}_\theta^\perp, \boldsymbol{w}\rangle = \langle \boldsymbol{u}_\theta^\perp, \boldsymbol{w}_i\rangle\}, \tag{VI.8}$$

which extends from the point $\left\langle \boldsymbol{u}_\theta^\perp, \boldsymbol{w}_i \right\rangle$ in the direction of the probe body $\boldsymbol{u}_\theta$. Every disc center $\boldsymbol{w}_i$ lies in the intersection of three such lines, corresponding to scan angles $\theta_1, \theta_2, \theta_3$. We argue that with probability one, the converse also holds: every intersection of three such lines is exactly the center $\boldsymbol{w}_i$ of some disc.

Without loss of generality, write $\boldsymbol{w}_{ij} = \ell_{(\theta_1,\boldsymbol{w}_i)} \cap \ell_{(\theta_2,\boldsymbol{w}_j)}$ as intersections of back projected lines from probe angle θ_1, θ_2 that passed different disc center locations $\boldsymbol{w}_i, \boldsymbol{w}_j$ respectively. Notice that $\boldsymbol{w}_{ij}$ is not the actual disc location for either $\boldsymbol{w}_i$ or $\boldsymbol{w}_j$ since there is no overlaps in the line scan R_1,R_2 from (VI.7). Suppose the point $\boldsymbol{w}_{ij}$ is in the third line set $\cup_k \ell_{(\theta_3,\boldsymbol{w}_k)}$, then there exists some disc center $\boldsymbol{w}_q$ such that the probe direction $\boldsymbol{u}_\theta$ is identical to the orientation of line formed by two points $\boldsymbol{w}_{ij}$ and $\boldsymbol{w}_q$. However since θ_3 is generated uniform randomly, we can conclude that for any i, j, q we have

$$\mathbb{P}\left[\exists\, q \in 1, \ldots, k \;s.t.\; \boldsymbol{w}_{ij} \in \ell_{(\theta_3,\boldsymbol{w}_q)}\right] = 0. \tag{VI.9}$$

The direction is not aligned with the line formed by $\boldsymbol{w}_{ij}$,$\boldsymbol{w}_q$ almost surely, implies that $\boldsymbol{w}_{ij}$ is not in line intersection for every $i \neq j$. Thus every intersection of three lines is one of the disc centers. The proof idea is demonstrated graphically in Figure 10. ■

References

[1] R. Wiesendanger and W. Roland, *Scanning probe microscopy and spectroscopy: methods and applications*. Cambridge university press, 1994.

[2] M. Lustig, D. L. Donoho, J. M. Santos, and J. M. Pauly, "Compressed sensing mri," *IEEE signal processing magazine*, vol. 25, no. 2, p. 72, 2008.

[3] V. Studer, J. Bobin, M. Chahid, H. S. Mousavi, E. Candes, and M. Dahan, "Compressive fluorescence microscopy for biological and hyperspectral imaging," *Proceedings of the National Academy of Sciences*, vol. 109, no. 26, pp. E1679–E1687, 2012.

[4] G. D. O'Neil, H.-W. Kuo, D. N. Lomax, J. Wright, and D. V. Esposito, "Scanning line probe microscopy: Beyond the point probe," *Analytical chemistry*, vol. 90, no. 19, pp. 11 531–11 537, 2018.

[5] A. J. Bard, L. R. Faulkner, J. Leddy, and C. G. Zoski, *Electrochemical methods: fundamentals and applications*. wiley New York, 1980, vol. 2.

[6] A. J. Bard, F.-R. F. Fan, D. T. Pierce, P. R. Unwin, D. O. Wipf, and F. Zhou, "Chemical imaging of surfaces with the scanning electrochemical microscope," *Science*, vol. 254, no. 5028, pp. 68–74, 1991.

[7] W. Rudin, *Real and complex analysis*. Tata McGraw-Hill Education, 2006.

[8] E. J. Candes, M. B. Wakin, and S. P. Boyd, "Enhancing sparsity by reweighted âĎŞ 1 minimization," *Journal of Fourier analysis and applications*, vol. 14, no. 5-6, pp. 877–905, 2008.

[9] T. Pock and S. Sabach, "Inertial proximal alternating linearized minimization (ipalm) for nonconvex and nonsmooth problems," *SIAM Journal on Imaging Sciences*, vol. 9, no. 4, pp. 1756–1787, 2016.

[10] V. S. J. W. Anna E. Dorfi, Han-Wen Kuo and D. V. Esposito, "Design and operation of a scanning electrochemical microscope for imaging with continuous line probes."